1 **Supporting Information**

2

3 **Reversible Solid Bromine Complexation into $Ti_3C_2T_x$ MXene Carriers: A Highly Active**

4 **Electrode for Bromine-based Flow Battery with Ultralow Self-discharge**

5 Luyin Tang,[ab] Tianyu Li,[a] Wenjing Lu*[a] and Xianfeng Li*[a]

6 [a] Dalian Institute of Chemical Physics, Chinese Academy of Sciences, Zhongshan Road 457, Dalian 116023,

7 P. R. China.

8 [b] University of Chinese Academy of Sciences, Beijing 100049, P. R. China.

9 * Correspondence author: luwenjing@dicp.ac.cn, lixianfeng@dicp.ac.cn

10

11 **Table of Contents**

1. Experimental Section

1.1 Preparation of $Ti_3C_2T_x$

$Ti_3C_2T_x$ was fabricated by etching Ti_3AlC_2 (Shanghai Yuehuan New Materials Technology Co., Ltd., 98%) in a 49 wt.% HF solution (Shanghai Yuehuan New Materials Technology Co., Ltd., 98%). Typically, 50 mL of 49 wt% HF solution was slowly added to 5 g Ti_3AlC_2 powders, and then the suspension was stirred in a water bath at 60^oC for 24 h. Afterward, the obtained $Ti_3C_2T_x$ was rinsed with deionized (DI) water several times until the pH of the solution reached about 7. Finally, the $Ti_3C_2T_x$ was dried under vacuum at $60\,^oC$ for 12 h.

1.2 Preparation of $Ti_3C_2T_x$-CTAB

$Ti_3C_2T_x$-CTAB was synthesized by a one-step process in which cetyl trimethyl ammonium bromide (CTAB, Shanghai Yuehuan New Materials Technology Co., Ltd., 98%) was intercalated into $Ti_3C_2T_x$ layers during etching. 50 mL of 49 wt% HF solution was slowly added to the mixture of 5 g Ti_3AlC_2 powders and 1.5 g CTAB, and then the suspension was stirred in a water bath at $60\,^oC$ for 24 h. Afterwards, the precipitate was repetitively centrifuged and washed with DI water until the pH value reached 7. Then the obtained $Ti_3C_2T_x$-CTAB was dried under vacuum at $60\,^oC$ for 12 h.

1.3 Preparation of $Ti_3C_2T_x$ or $Ti_3C_2T_x$-CTAB modified carbon felt

First, the prepared $Ti_3C_2T_x$ and 0.05 wt.% Nafion solution were dispersed into 6 mL of isopropanol to form a uniformly distributed suspension by strong sonication. The composite electrode was prepared by spraying the above suspension on the surface of a piece of $3 \times 3\ cm^2$ nonpolar carbon felt (PCF) with a loading of ~5 mg cm^{-2}. The obtained electrode was denoted as TiCF. The preparation of $Ti_3C_2T_x$-CTAB modified PCF was the same as above, except that $Ti_3C_2T_x$ was replaced by $Ti_3C_2T_x$-CTAB (denoted as TiCCF).

1.4 Preparation of $Ti_3C_2T_x$ or $Ti_3C_2T_x$-CTAB modified glassy carbon

2.5 mg $Ti_3C_2T_x$-CTAB, 0.5 mL isopropyl alcohol and 10 µL of 0.05 wt.% Nafion solution were ultrasonically mixed to form a uniform slurry. 10 µL of the slurry was absorbed by a microsyringe and transferred to the pristine glassy carbon (PGC) electrode, and the modified electrode (denoted as TiCGC) was obtained after the solvent was volatilized completely. The preparation of $Ti_3C_2T_x$ modified PGC was the same as above, except that $Ti_3C_2T_x$-CTAB was replaced by $Ti_3C_2T_x$ (denoted as TiGC).

1.5 Materials characterization

The morphology and element distribution of the prepared materials were detected by scanning electron microscopy (SEM, JSM-7800F and SUI510) equipped with an energy dispersive X-ray spectroscope (EDS). The X-ray diffraction (XRD) patterns were examined by an X-ray diffractometer (D8 ADVANCE ECO; RIGAKU, Japan) with a monochromatic Cu-Kα radiation source at 40 kV and 40 mA and a scan rate of $10°\ min^{-1}$. X-ray photoelectron spectroscopy (XPS) was performed using a Thermo Scientific^{TM} K-Alpha^{TM+} spectrometer equipped with a monochromatic Al Kα X-ray source (1486.6 eV) operating at 100 W and Thermo Scientific ESCALAB Xi$^+$. A sessile drop method was utilized to measure the electrode-electrolyte contact angle with the aqueous electrolyte (2 M $ZnBr_2$ + 3 M KCl + 0.4 M N-methylethylpyrrolidinium bromide (MEPBr)) (JC2000A, POWEREACH®, Shanghai Zhongchen Digital Technic Apparatus Co. Ltd., China). N_2 adsorption/desorption measurements were carried out using a gas adsorption analyzer (ASAP2010/ASAP2010M) to study the specific surface area of the material. The BET (Brunauer-Emmett-Teller) method was used to calculate the specific surface area of the adsorption branches.

1.6 Electrochemical measurement

Cyclic voltammetry (CV), linear sweep voltammetry (LSV) and electrochemical impedance spectra (EIS) of GC, TiGC, TiCGC together with PCF, TiCF and TiCCF were carried out in a typical three-electrode system measurement using a Gamry Multichannel System installation (Gamry Interface 1000 or Gamry Reference 3000). A graphite plate (2×2 cm^2) was used as the counter electrode and an Ag/AgCl electrode (0.198 V vs. SHE) was used as the reference electrode. As for electrode samples, the working electrode was made by cutting PCF, TiCF and TiCCF into a cylinder, which had a diameter of 6 mm and a thickness of 2 mm. The CV test was carried out from 0 to 1 V (vs. Ag/AgCl) in 2 M $ZnBr_2$ + 3 M KCl or 2 M $ZnBr_2$ + 3 M KCl + 0.4 M MEPBr at a scan rate of 10 mV s^{-1}. The CV tests at different scan rates to determine reversibility were performed in 0.05 M $ZnBr_2$+ 0.05 M H_2SO_4 from 0 to 1.2 V (vs. Ag/AgCl). The CV stability was tested in 2 M $ZnBr_2$+ 3 M KCl for 500 cycles at a high scan rate of 50 mV s^{-1}. The LSV test was carried out at a scan rate of 1 mV s^{-1} in 2 M $ZnBr_2$ + 3 M KCl or 2 M $ZnBr_2$ + 3 M KCl + 0.4 M MEPBr. EIS tests were performed in 2 M $ZnBr_2$ + 3 M KCl or 2 M $ZnBr_2$ + 3 M KCl + 0.4 M MEPBr, with a frequency range of 0.1-10^5 Hz and an amplitude of 5 mV.

1.7 *In-situ* Raman spectroscopy test

In-situ Raman measurement (NanoWizard Ultra Speed & inVia Raman, Laser wavelength: 532 nm, exposure time: 50 s) was used to study the electrochemical reaction process on different electrodes. Two polar plates with holes were clamped with a Daramic® HP membrane (Polypore (Shanghai) Membrane Products Co., Ltd, China) and two 3×3 cm^2 electrodes to assemble a zinc-bromine single cell.[1] All of these parts were fixed between two stainless steel plates with holes, allowing the laser to hit the electrode surface. The electrodes were cut into thin sheets of about 1 mm with an effective area of 3 x 3 cm^2 and should be fully immersed in the 2 M $ZnBr_2$ + 3 M KCl + 0.4 M MEPBr solution before assembling the cell. The compression ratio of the electrodes was around 50%. The assembled battery was charged at a constant current of 10 mA for 30 minutes, and the discharge cut-off voltage was set to 0.8 V (a LAND battery test instrument: CT2001A, Wuhan, China).

1.8 Bromine entrapping/retaining ability measurement

i) For Fig. 4a, 0.05g $Ti_3C_2T_x$ or $Ti_3C_2T_x$-CTAB was added to a 10 mL 0.2 M bromine solution. For Fig. S10a, 5 mM MEPBr or CTAB was added to a 10 mL 0.2 M bromine solution (labeled as solution A and B, respectively). For Fig. S10b, 1 mM MEPBr or CTAB was added to a 10 mL 10 mM bromine solution (labeled as solution A and B, respectively). Digital photographs were taken to record the color change of the solution over time.

ii) For Fig. 2d, a UV-vis spectrometer (UV-Vis, TU-1901, Beijing Purkinje General Instrument Co., Ltd.) was used to record the UV spectra of the 10 mM bromine solution before and after the immersion of 1 mM MEPBr and CTAB (labeled as solution A and solution B), respectively. For Fig. 4c, a piece of the electrode (PCF, TiCF or TiCCF) was cut into a cylinder with a diameter of 6 mm and a thickness of 2 mm, followed by soaking in a 10 mL 10 mM bromine solution for some time. Then the UV spectra of the bromine solution before and after the immersion of different electrodes were recorded.

iii) The capacibity to inhibit bromine diffusion of $Ti_3C_2T_x$ or $Ti_3C_2T_x$-CTAB was evaluated by the rotating ring-disk electrode (RRDE) technique using a Gamry Multichannel System installation (Gamry Interface 1000 and Gamry Reference 3000). The mixture of 2.5 mg of prepared material, 0.5 mL isopropyl alcohol and 10 μL of 0.05 wt.% Nafion solution was sonicated for several minutes. The working electrode was coated with the

1 above uniform slurry, where Pt and glassy carbon (D = 6 mm) were used as the ring and the disk,

2 respectively. The counter electrode was a graphite plate (1 x 1 cm^2) and the reference electrode was an

3 Ag/AgCl electrode (0.198 V vs. SHE). The oxidation current on the disk electrode was set at 1 mA and held

4 for 60 s, and the reduction potential on the ring electrode was maintained at 0.5 V (vs. Ag/AgCl). The

5 experiment was carried out in an electrolyte of 2 M ZnBr$_2$ + 0.4 M MEPBr with a rotational speed of 2000

6 rpm.

7 iv) The visualization experiments were carried out in 2 M ZnBr$_2$ + 3 M KCl using Gamry Interface 1000 to

8 observe bromine diffusion. The electrodes (PCF, TiCF and TiCCF) were cut into 3 × 3 cm^2 with a thickness of

9 2 mm to be used as the cathode and anode, respectively. After charging at 0.36 A for 5 and 10 minutes,

10 photos were taken to record the color changes of the solution.

11 **1.9 Density functional theory calculations**

12 Density functional theory (DFT) calculations were implemented by the Vienna Ab-initio Simulation Package

13 (VASP)[2] with the projector-augmented wave (PAW)[3] method. All calculations were based on the same

14 generalized gradient approximation (GGA)[4] method. Perdew-Burke-Ernzerhof (PBE)[5] functional was applied

15 to cope with the exchange-correlation term. Van der Waals interaction was taken into account at DFT-D3[6]

16 with Becke-Jonson (BJ)[7, 8] damping level. The plane wave cutoff was set to 500 eV. The Brillouin zone

17 integration was carried out with 3×3×1 Gamma point for Zn-H$_2$O and Zn-DMSO, but 2×3×1 Gamma point

18 for the Zn-VISP system. The convergence thresholds for energy and the convergence thresholds for force

19 were set at 10^{-4} eV and 0.05 eV·Å^{-1} during ion relaxation, respectively.

20 **1.10 Full battery test of a zinc-bromine flow battery**

21 A zinc-bromine flow battery (ZBFB) with an effective electrode area of 3 x 3 cm^2 was assembled in the same

22 way as *in-situ* Raman tests. Differently, the electrode compression ratio was around 74% and the electrode

23 thickness was 5 mm. A mixture of 60 mL of 2 M ZnBr$_2$ + 3 M KCl or 2 M ZnBr$_2$ + 3 M KCl + 0.4 M MEPBr was

24 used as both the positive and negative electrolytes. The flow rate of electrolytes was maintained at 50−60

25 mL min^{-1}. ZnBr$_2$ was the active material and KCl served as the supporting electrolyte to improve the

26 conductivity of the electrolyte. MEPBr was one kind of bromine complexing agent (BCA) that complexed

27 with bromine to inhibit the bromine crossover. The ZBFBs operated at different current densities ranging

28 from 80 to 180 mA cm^{-2} at room temperature. All measurements were performed under an areal capacity

29 of 40 mAh cm^{-2} with Arbin BT 2000 or Neware battery test system (CT-4008T-5V12A-204n-F, Shenzhen,

30 China). The charge process was controlled by the charge time to keep the charge capacity constant, while

31 the discharge process was terminated by setting the cut-off voltage to 0.8 V. In the self-discharge

32 performance test, 15 cycles of running were followed by 24-h placement and then continued operation at

33 80 mA cm^{-2}. The CE of the 16th cycle was considered as the capacity retention rate under such constant

34 capacity charge and cut-off voltage discharge modes.

35

36

37

38

39

1

2. Supplementary Figures
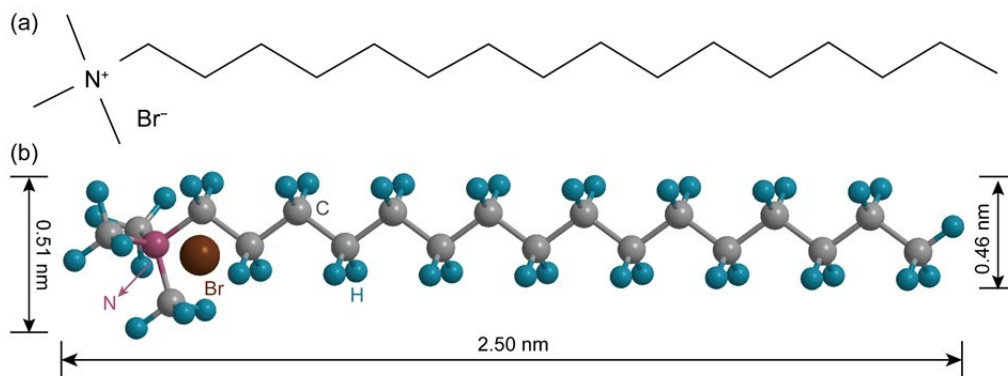
Fig. S1 The formula and 3D structure of CTAB.

CTAB is a cationic surfactant with a large volume that has good coordination with nonionic and zwitterionic surfactants, making it an ideal intercalating agent (Fig. S1). At the same time, the $-N^+-Br^-$ group causes that CTAB can play a role in complexing bromine species, namely acting as a BCA. From Fig. S1, the dimensional schematic of CTAB showed a length of 2.5 nm as well as the corresponding widths of the two sides of 0.51 and 0.46 nm, respectively.[9]

3
4
5
6
7
8
9
10
11
12
13
14
15
16
17
18
19
20
21
22
23
24
25
26
27
28
29

1
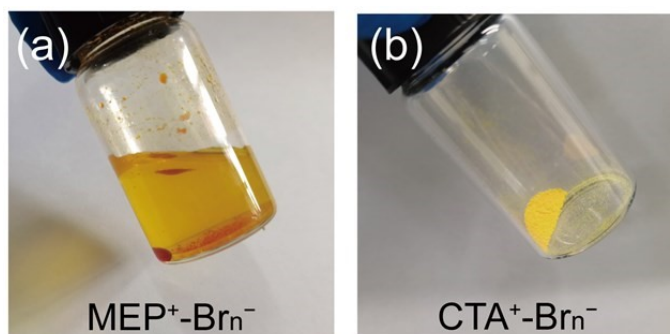
Fig. S2 The comparison of MEP$^+$-Br$_n^-$ and CTA$^+$-Br$_n^-$ complexes.

From Fig. S2, the commonly used MEPBr complexed with bromine to form oily MEP$^+$-Br$_n^-$, while CTA$^+$-Br$_n^-$ was solid complexes.

5

6

7

8

9

10

11

12

13

14

15

16

17

18

19

20

21

22

23

24

25

26

27

28

29

30

31

32

33

1 **Table S1 Comparison of previously reported current densities and corresponding efficiencies of ZBFBs.**

Current density/ mA cm^{-2}	CE/ %	VE/ %	EE/ %	References
20	90.71	80.7	73.2	[10]
20	95	85	80.75	[11]
20	95	86	78	[12]
30	95.52	87.02	83.12	[13]
30	99	83	82	[14]
50	99.96	88.06	88.02	[15]
80	95.81	79.32	76.02	[16]
80	96.62	82.9	80.1	[17]
80	98	82.65	81.0	[18]
80	99	81	80.19	[19]
80	99.4	83	82.5	[20]
120	99	69.7	69	[21]
180	98.29	60.38	59.35	[22]
180	99.2	64.01	63.5	[23]
180	97.26	64.85	63.07	[1]
180	98.95	66.76	66.06	This work

2
3
4
5
6
7
8
9
10
11
12
13
14
15
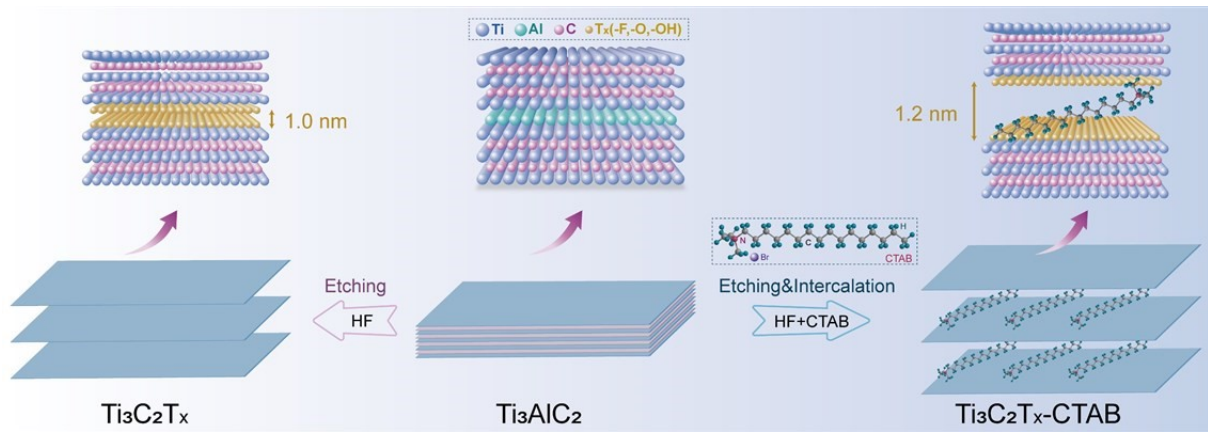
Fig. S3 Schematic illustration for the synthesis of Ti$_3$C$_2$T$_x$ MXene and Ti$_3$C$_2$T$_x$-CTAB.

Different from the conventional etching method followed by an intercalating process, the mixture of Ti$_3$AlC$_2$ and CTAB powders was directly treated with a concentrated HF solution.
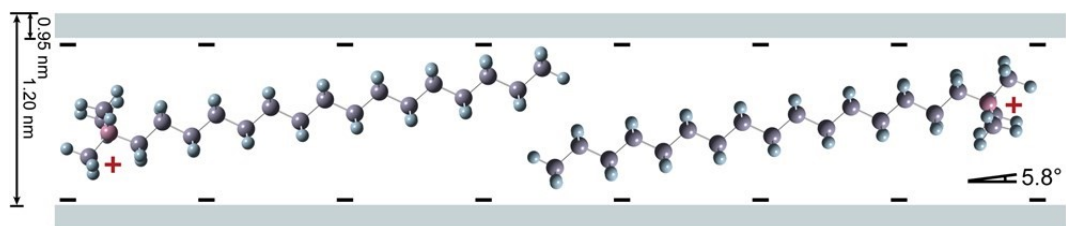
Fig. S4 Possible position of CTA$^+$ in the interlayer of Ti$_3$C$_2$T$_x$ MXene.

During the intercalation process, CTAB was self-assembled and intercalated into the interlayer of negatively charged Ti$_3$C$_2$T$_x$ MXene by the electrostatic interaction, increasing the interlayer spacing.[24] Since the layer spacing of Ti$_3$C$_2$T$_x$-CTAB was 1.20 nm and the thickness of the Ti$_3$C$_2$T$_x$ monolayer was about 0.95 nm, CTA$^+$ was considered to be inserted at an inclination of 5.8° to the wide plane (Fig. S4).
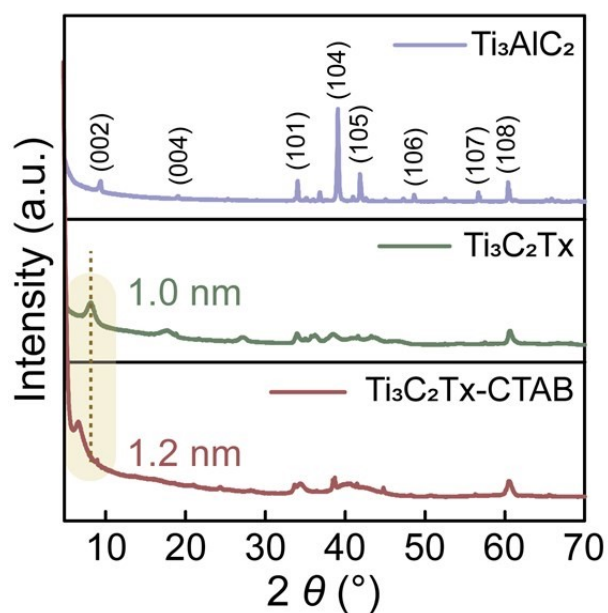
Fig. S5 The XRD patterns of Ti$_3$AlC$_2$, Ti$_3$C$_2$T$_x$ and Ti$_3$C$_2$T$_x$-CTAB.

As shown in Fig. S5, the (104) peak of Ti$_3$AlC$_2$ located at 39.3° disappeared in the XRD patterns of Ti$_3$C$_2$T$_x$ and Ti$_3$C$_2$T$_x$-CTAB, indicating that the Al layers were completely removed after HF etching. According to Bragg's equation, the interlayer spacing of Ti$_3$C$_2$T$_x$ was 1.0 nm. When CTAB was added simultaneously for the intercalation during the etching process, the peak of (002) was shifted to 7.2°, leading to a increased interlayer spacing of 1.2 nm.

1

2

3

4

5

6

7

8

9

10

11

12

13

14

15

16

17

18

19

20

21

22

23

24

25

26
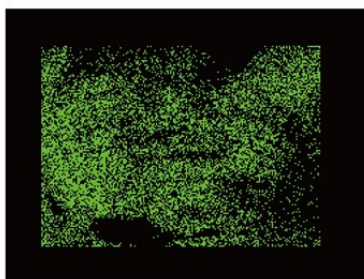
1

2 **Fig. S6 EDS mapping image of F element in Ti$_3$C$_2$T$_x$-CTAB.**
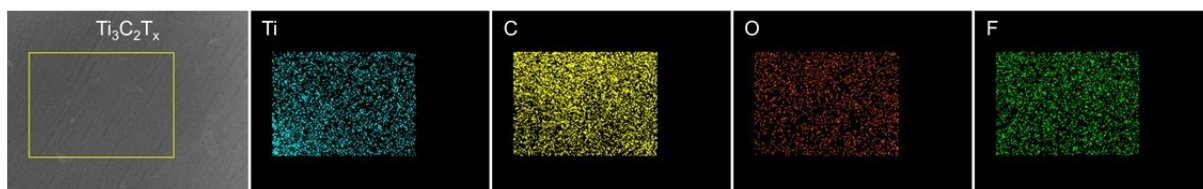
3

4 **Fig. S7 EDS mapping images of Ti$_3$C$_2$T$_x$ MXene.**

5

6

7

8

9

10

11

12

13

14

15

16

17

18

19

20

21

22

23

24

25

26

27

28

29

30

31
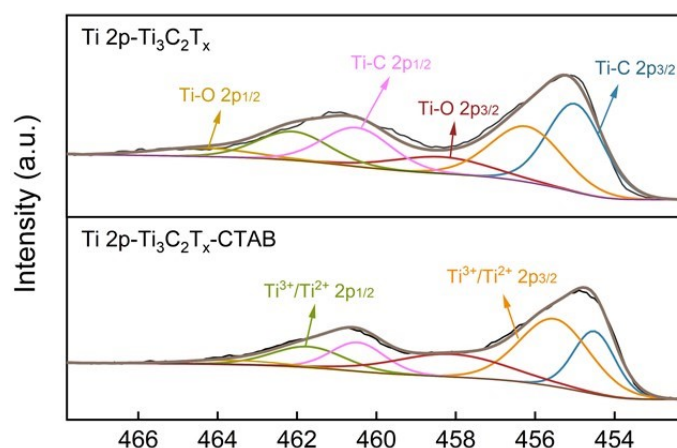
Fig. S8 High-resolution Ti 2p XPS spectra of $Ti_3C_2T_x$ and $Ti_3C_2T_x$-CTAB.

As shown in Fig. S8, the high-resolution Ti 2p signals could be deconvoluted into six peaks for Ti-C $2p_{3/2}$, Ti^{2+}/Ti^{3+} $2p_{3/2}$, Ti-O $2p_{3/2}$, Ti-C $2p_{1/2}$, Ti^{2+}/Ti^{3+} $2p_{1/2}$, and Ti-O $2p_{1/2}$, respectively.[25, 26] The proportion of Ti-C bond in $Ti_3C_2T_x$-CTAB obviously decreased (from 47.05% to 31.22%) due to the fact that the insertion of CTAB resulted in partial destruction and conversion of Ti-C to Ti^{2+}, Ti^{3+} and Ti^{4+} (Table. S2).[27] This was also the reason for the increased proportion of Ti^{2+}/Ti^{3+} (from 37.63% to 46.74%) and Ti-O bonds (from 15.32% to 22.03%) in the Ti 2p XPS spectra of $Ti_3C_2T_x$-CTAB. These results further confirmed the successful intercalation of CTAB into $Ti_3C_2T_x$ MXene (Table. S2).

Table S2 The proportion of each Ti 2p peak in $Ti_3C_2T_x$ and $Ti_3C_2T_x$-CTAB (based on Fig. S8).

Peaks Ratio (%)	Ti-C	Ti^{2+}/Ti^{3+}	Ti-O
$Ti_3C_2T_x$	47.05	37.63	15.32
$Ti_3C_2T_x$-CTAB	31.22	46.74	22.03

1
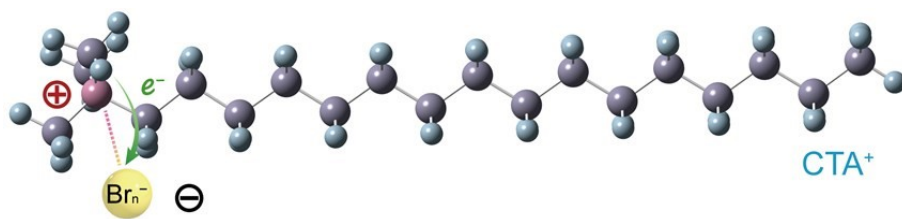
2 **Fig. S9 Electron transfer after CTAB complexing with bromine.**

3

4

5

6

7

8

9

10

11

12

13

14

15

16

17

18

19

20

21

22

23

24

25

26

27
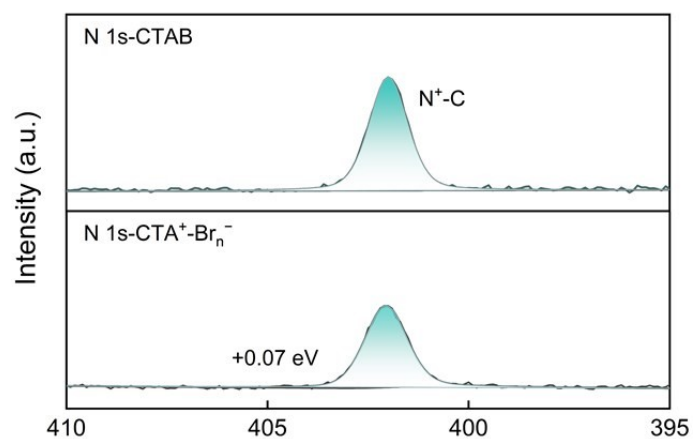
Fig. S10 High resolution N 1s XPS spectra of CTAB and CTA$^+$-Br$_n^-$.
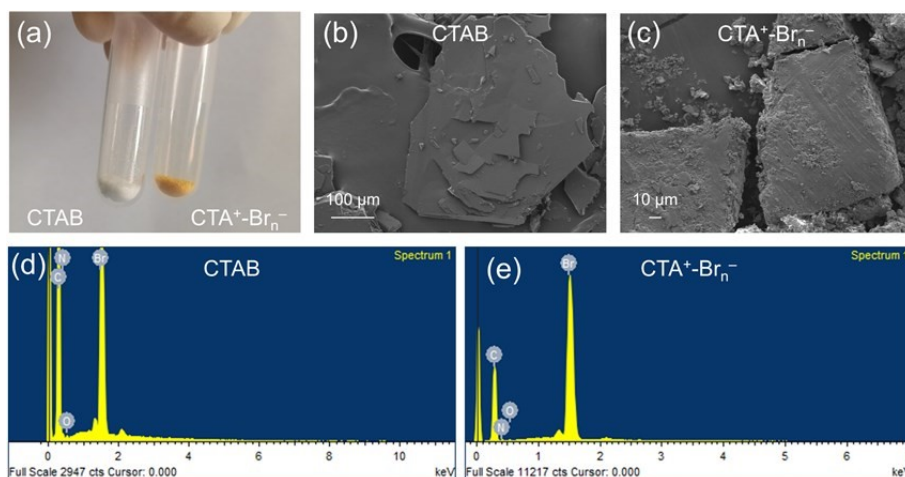
Fig. S11 (a) Photographs of CTAB and CTA$^+$-Br$_n^-$. SEM images of (b) CTAB and (c) CTA$^+$-Br$_n^-$. EDS energy spectra of (d) CTAB and (e) CTA$^+$-Br$_n^-$.

As shown in Fig. S11a, CTAB was a white crystal whose color turned yellow after complexing with bromine. Additionally, the surface of CTA$^+$-Br$_n^-$ became rougher than that of CTAB (Fig. S11b–c). As expected, the bromine content in CTA$^+$-Br$_n^-$ was obviously higher than that in CTAB based on such a strong solid complexation effect (Fig. S11d–e and Table S3).

Table S3 Elemental analysis of CTAB and CTA$^+$-Br$_n^-$ (based on Fig. S11d–e).

Element Atomic%	C K	N K	O K	Br L	Total
CTAB	88.95	6.67	0.86	3.52	100
CTA$^+$-Br$_n^-$	85.97	5.89	0.79	7.35	100
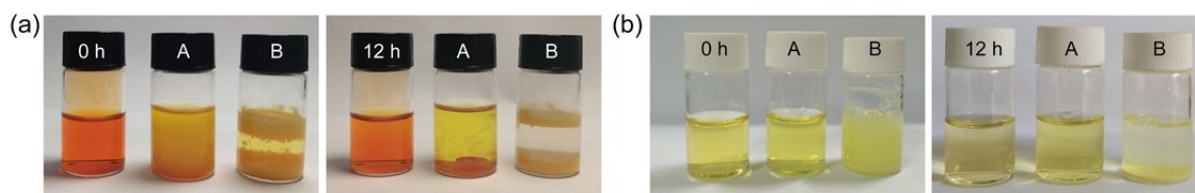
Fig. S12 Digital photographs of the color change of (a) the 0.2 M bromine solution over time after the addition of 5 mM MEPBr (solution A) or CTAB (solution B) and (b) the 10 mM bromine solution over time after the addition of 1 mM MEPBr (solution A) or CTAB (solution B).

The aqueous solution containing MEPBr (labelled as solution A) still kept yellow after 12 h, while that of containing CTAB (labelled as solution B) was almost colorless no matter with a low or high bromine concentration. That was because that more bromine could be captured in the solid complexes (Fig. S12). In addition, the UV-vis spectra quantitatively detected the bromine species in solutions A and B (Fig. 2d and Fig. S12b), further indicating the stronger bromine complexation effect of CTAB than that of MEPBr. Notably, considering the detection range of the UV-vis spectrometer, the bromine specie in the 10 mM bromine solution after adding MEPBr or CTAB was measured (Fig. 2d).

1   **Table S4 The Gibbs free energy of all the components in complex formation.**

| Br^- (a.u.)	Br_2 (a.u.)	Br_3^- (a.u.)	Br_5^- (a.u.)
-2574.3731	-5148.4005	-7722.7913	-12871.1917
MEP^+ (a.u.)	MEPBr (a.u.)	$MEP^+\text{-}Br_3^-$ (a.u.)	$MEP^+\text{-}Br_5^-$ (a.u.)
-330.7442	-2905.1167	-8053.5286	-13201.9256
CTA^+ (a.u.)	CTAB (a.u.)	$CTA^+\text{-}Br_3^-$ (a.u.)	$CTA^+\text{-}Br_5^-$ (a.u.)
-803.2891	-3377.6615	-8526.0753	-13674.4723

2   We assumed two possible ways of generating $MEP^+\text{-}Br_n^-$ and $CTA^+\text{-}Br_n^-$ as well as calculated the ΔGs at each

3   step.

4   (i) The formation process of $MEP^+\text{-}Br_n^-$ and $CTA^+\text{-}Br_n^-$ in the first way and corresponding ΔGs

5   (a) $MEP^+ + Br^- + Br_2 \rightleftharpoons MEP^+\text{-}Br_3^-$ (1)
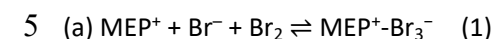
6   ΔG_1 = -8053.5286 – (-2574.3731) – (-5148.4005) – (-330.7442) = -0.0108 (a.u.)

7   Corrected ΔG_1 = -0.0108×2626.7548= -28.37 (kJ mol^{-1})

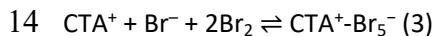8 $MEP^+ + Br^- + 2Br_2 \rightleftharpoons MEP^+\text{-}Br_5^-$ (3)
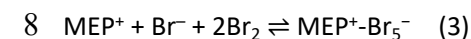
9   ΔG_3 = -13201.9256 – (-2574.3731) – (-5148.4005)*2 – (-330.7442) = -0.0073 (a.u.)

10   Corrected ΔG_3 = -0.0073×2626.7548= -19.18 (kJ mol^{-1})

11   (b) $CTA^+ + Br^- + Br_2 \rightleftharpoons CTA^+\text{-}Br_3^-$ (1)
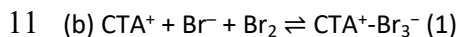
12    $\Delta G_1'$ = -8526.0753 – (-2574.3731) – (-5148.4005) – (-803.2891) = -0.0126 (a.u.)

13   Corrected $\Delta G_1'$ = -0.0126×2626.7548= -33.10 (kJ mol^{-1})

14    $CTA^+ + Br^- + 2Br_2 \rightleftharpoons CTA^+\text{-}Br_5^-$ (3)

15    $\Delta G_3'$ = -13674.4723 – (-2574.3731) – (-5148.4005)*2 – (-803.2891) = -0.0091   (a.u.)

16   Corrected $\Delta G_3'$ = -0.0091×2626.7548= -23.90 (kJ mol^{-1})

17   (ii) The formation process of $MEP^+\text{-}Br_n^-$ and $CTA^+\text{-}Br_n^-$ in the second way and corresponding ΔGs

18   (a) $MEP^+\text{-}Br^- + Br_2 \rightleftharpoons MEP^+\text{-}Br_3^-$ (1)
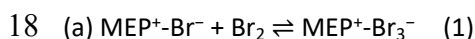
19   ΔG_1 = -8053.5286 – (-2905.1167) – (-5148.4005) = -0.0114 (a.u.)

20   Corrected ΔG_1 = -0.0114×2626.7548= -29.95 (kJ mol^{-1})

21    $MEP^+\text{-}Br_3^- + Br_2 \rightleftharpoons MEP^+\text{-}Br_5^-$ (2)
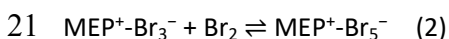
22   ΔG_2 = -13201.9256 – (-8053.5286) – (-5148.4005) = 0.0035 (a.u.)

23   Corrected ΔG_2 = 0.0035×2626.7548 = 9.19 (kJ mol^{-1})

24   (b) $CTA^+\text{-}Br^- + Br_2 \rightleftharpoons CTA^+\text{-}Br_3^-$ (1)
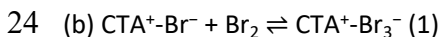
25    $\Delta G_1'$ = -8526.0753 – (-3377.6615) – (-5148.4005) = -0.0133 (a.u.)

26   Corrected $\Delta G_1'$ = -0.0126×2626.7548= -34.94 (kJ mol^{-1})

27    $CTA^+\text{-}Br_3^- + Br_2 \rightleftharpoons CTA^+\text{-}Br_5^-$ (2)
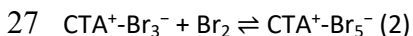
28    $\Delta G_2'$ = -13674.4723 – (-8526.0753) – (-5148.4005) = 0.0035 (a.u.)

29   Corrected $\Delta G_2'$ = 0.0035×2626.7548 = 9.19 (kJ mol^{-1})

30   The theoretical results showed that the formation of $CTA^+\text{-}Br_n^-$ in both ways were all easier than that of

31    $MEP^+\text{-}Br_n^-$, implying its stronger complexation effect.
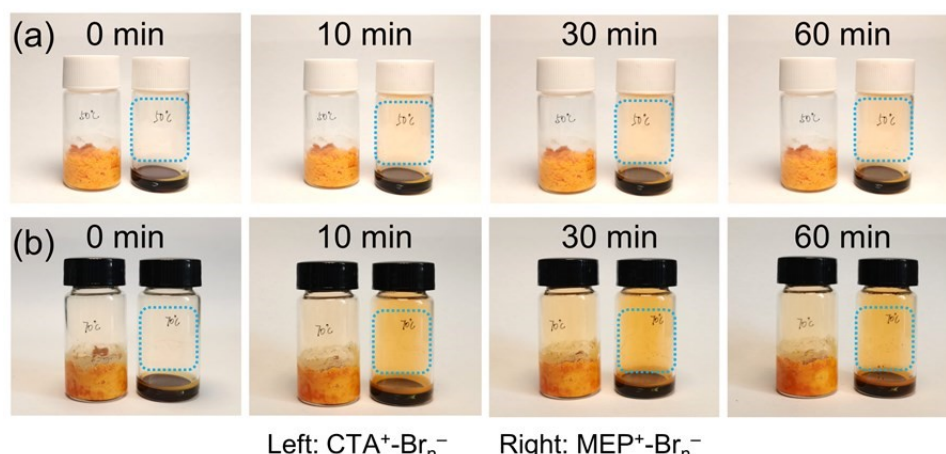
Left: CTA$^+$-Br$_n^-$ Right: MEP$^+$-Br$_n^-$

Fig. S13 Photographs of CTA$^+$-Br$_n^-$ and MEP$^+$-Br$_n^-$ after being heated at (a) 50°C and (b) 70°C for different times.

The CTA$^+$-Br$_n^-$ and MEP$^+$-Br$_n^-$ were heated at 50°C for a certain time to test their stability (Fig. S13a). When the heating process began, bromine immediately volatilized from the oily MEP$^+$-Br$_n^-$ complexes, and plentiful bromine vapor was produced in MEP$^+$-Br$_n^-$ with prolonging the heating time. On the contrary, there was no obvious bromine volatilizing from the solid CTA$^+$-Br$_n^-$ complexes as increasing the heating time, indicating its excellent stability, namely ultrastrong bromine complexation capacity of CTAB (Fig. S13a). Similar phenomenon was also observed when MEP$^+$-Br$_n^-$ and CTA$^+$-Br$_n^-$ were heated at a higher temperature of 70°C, further proving the better stability of CTA$^+$-Br$_n^-$ (Fig. S13b).
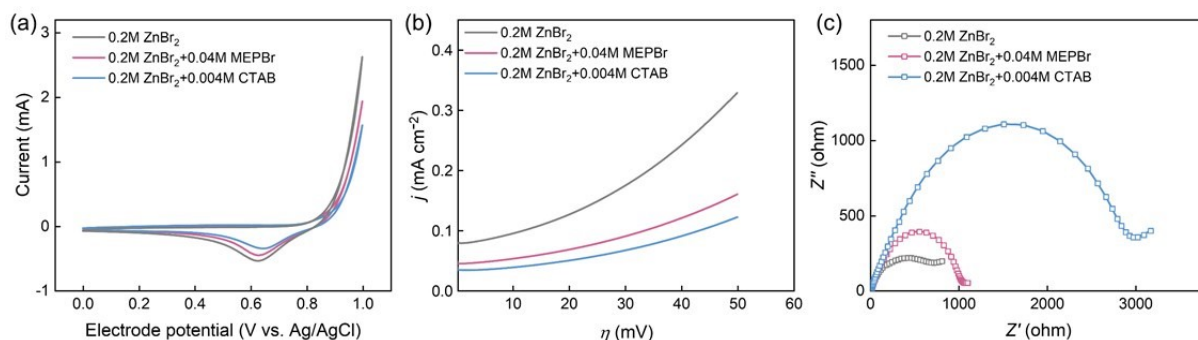
Fig. S14 The electrochemical performance of GC electrode in the electrolytes with MEPBr or CTAB as additives. (a) CV curves of at the scan rate of 10 mV s^{-1}. (b) LSV curves at the scan rate of 1 mV s^{-1}. (c) Nyquist plots.

The solid bromine complexes in electrolytes will block the pipeline and affect electrolyte flowing, which is consequently commonly applied to single-flow or static Br-FBs rather than dual-flow batteries.[28, 29] Moreover, as shown in Fig. S14, even though the CTAB content was much lower than MEPBr, the electrolyte with CTAB as the additive showed lower electrochemical activity, slower reaction kinetics and higher impedance than that with MEPBr. Therefore, CTAB cannot be used directly as an electrolyte additive for Br-FBs.
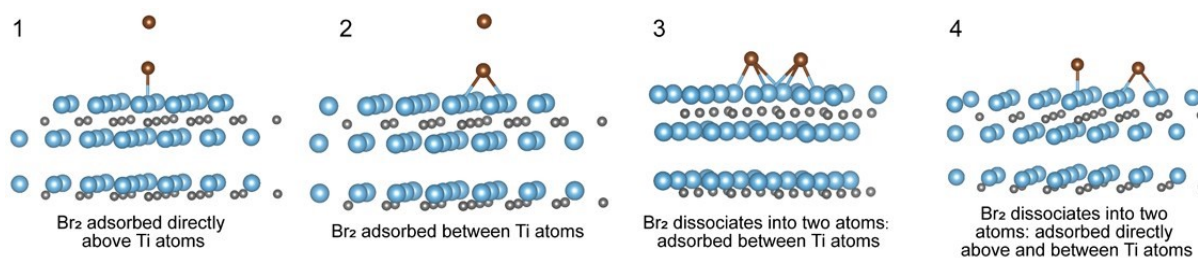
Fig. S15 Four structures of Ti$_3$C$_2$T$_x$ surfaces which absorb bromine molecules (blue spheres: Ti atoms; gray spheres: C atoms; brown spheres: Br atoms).

According to previous reports, the optimized interaction sites of Br species on Ti$_3$C$_2$T$_x$ MXene were located above Ti, C, and O atoms, respectively.[30, 31] Although the calculated adsorption energies (ΔEs) for all sites were negative, Ti sites demonstrated the lowest ΔEs.[30] Considering that Ti atoms were the optimal adsorption sites, we further studied the optimal bromine adsorption mode at Ti sites in this work. As shown in Fig. S15, a Br$_2$ molecule could be adsorbed directly above or between Ti atoms, and it could also dissociate into two atoms adsorbed between Ti atoms or one of them could be adsorbed between Ti atoms and the other adsorbed directly above Ti atoms. The adsorption behavior occurred most readily when a Br$_2$ molecule was dissociated into two atoms and then adsorbed, requiring the lowest energy.

1
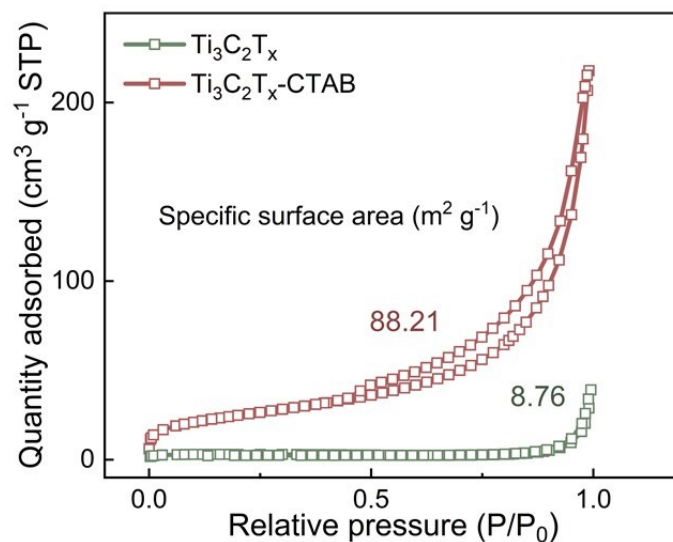
2 **Fig. S16 N$_2$ sorption isotherms curves of Ti$_3$C$_2$T$_x$ and Ti$_3$C$_2$T$_x$-CTAB.**

3 The intercalation of CTAB increased the interlayer spacing and effectively enlarged the specific surface area,

4 which was calculated to be 8.76 m^2 g^{-1} for Ti$_3$C$_2$T$_x$ and 88.21 m^2 g^{-1} for Ti$_3$C$_2$T$_x$-CTAB (Fig. S16). As a result,

5 Ti$_3$C$_2$T$_x$-CTAB was able to expose more active sites and exhibit more efficient ion/electron transportation.

6

7

8

9

10

11

12

13

14

15

16

17

18

19

20

21

22

23
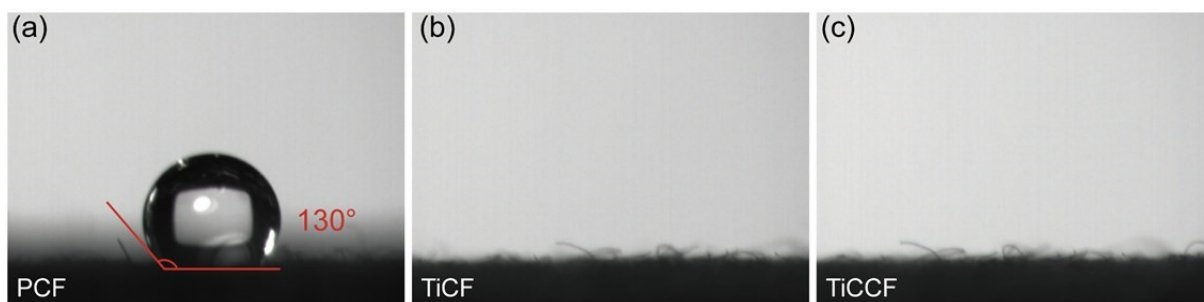
Fig. S17 Electrolyte contact angles of (a) PCF; (b) TiCF; and (c) TiCCF.

To measure the electrolyte contact angles of $Ti_3C_2T_x$ and $Ti_3C_2T_x$-CTAB, the contact angle measurements with the aqueous electrolytes were conducted on PCF, TiCF and TiCCF (using PCF as the substrate). As shown in Fig. S17, the electrolyte contact angle of PCF (130°) was large, while the electrolyte immediately permeated into TiCF and TiCCF, indicating their ultrahigh electrolyte wettability.

1 **Table S5 Values of R_p, i_0 and k_0.**

Materials	R_p/ Ω cm^2	i_0/ A cm^{-2} × 10^{-3}	k_0/ cm s^{-1} × 10^{-6}
PGC	11.36	1.13	1.46
TiGC	5.67	2.26	2.93
TiCGC	4.74	2.71	3.51

2 The values of R_p, i_0 and k_0 were calculated from the following equations:[18]

3 $$R_p = \frac{\eta}{j}$$

4 $$i_0 = \frac{RT}{nFR_p}$$

5 $$k_0 = \frac{i_0}{nFC_0}$$

6 R_p: Polarization impedance

7 η: Overpotential

8 j: Current density

9 i_0: Exchange current density

10 R: Ideal gas constant

11 T: Kelvin temperature

12 n: Electron transfer number

13 F: Faraday constant

14 k_0: Constant of reaction rate

15 C_0: Reactant concentration

16

17

18

19

20

21

22

23

24

25

26

1
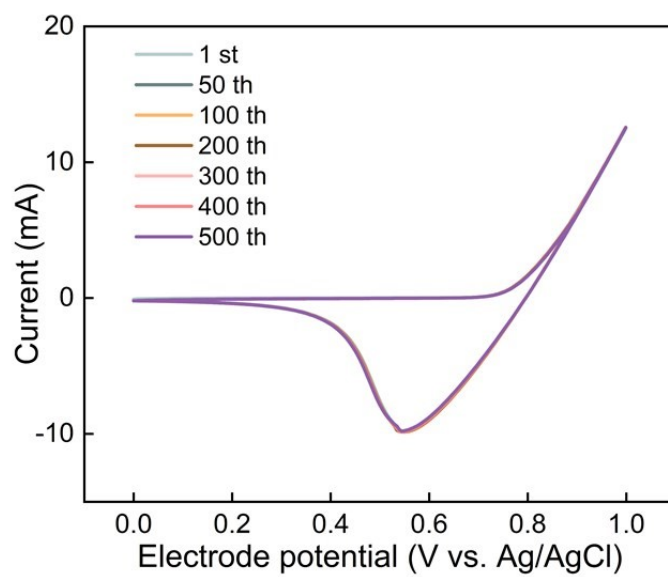
Fig. S18 CV stability test of TiCGC at the scan rate of 50 mV s^{-1} in the electrolyte of 2 M ZnBr$_2$ + 3 M KCl (vs. Ag/AgCl).

4
5
6
7
8
9
10
11
12
13
14
15
16
17
18
19
20
21
22
23
24
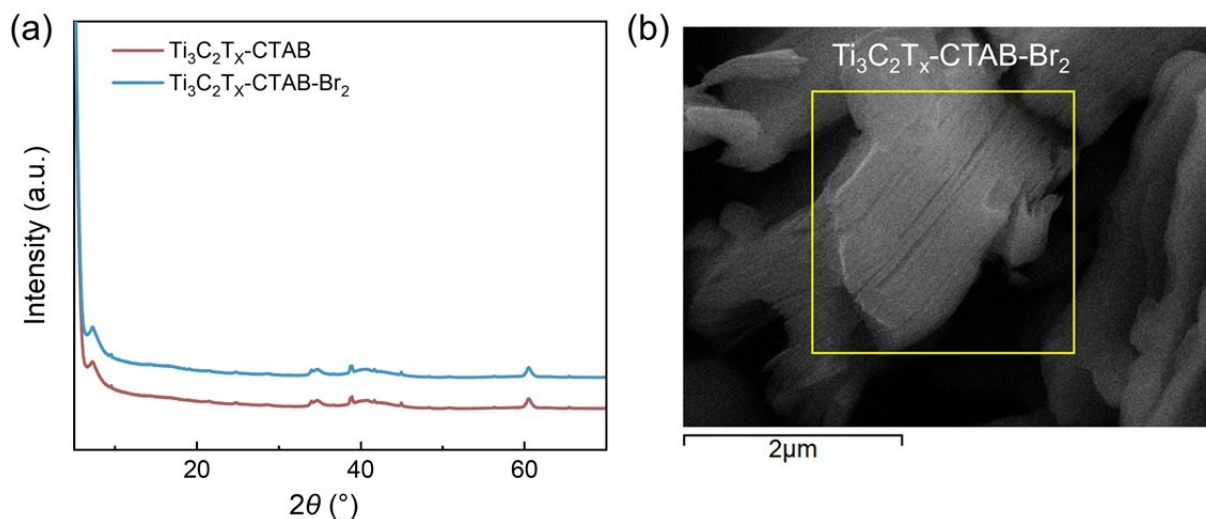
Fig. S19 (a) The XRD patterns of Ti$_3$C$_2$T$_x$-CTAB and Ti$_3$C$_2$T$_x$-CTAB-Br$_2$ (after Ti$_3$C$_2$T$_x$-CTAB reacting with bromine species). (b) SEM image of Ti$_3$C$_2$T$_x$-CTAB-Br$_2$.

As shown in Fig. S19a, there was no significant difference in the XRD patterns of Ti$_3$C$_2$T$_x$-CTAB and Ti$_3$C$_2$T$_x$-CTAB-Br$_2$, namely, the layer spacings had not been changed after reacting with bromine. In addition, Ti$_3$C$_2$T$_x$-CTAB-Br$_2$ also showed the accordion structure like Ti$_3$C$_2$T$_x$-CTAB (Fig. 1d and S19b). These results indicated that CTAB intercalation endowed Ti$_3$C$_2$T$_x$-CTAB with high oxidization stability and anti-stack ability.
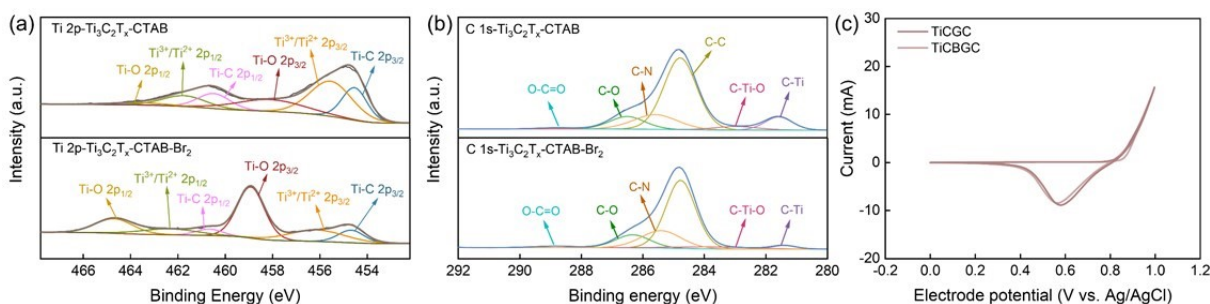
Fig. S20 High-resolution (a) Ti 2p and (b) C 1s XPS spectra of $Ti_3C_2T_x$-CTAB and $Ti_3C_2T_x$-CTAB-Br$_2$. (c) CV curves of TiCGC and TiCBGC in 2 M ZnBr$_2$ + 3 M KCl + 0.4 M MEPBr at the scan rate of 10 mV s^{-1}.

As shown in Fig. S20a, the high-resolution Ti 2p signal could be deconvoluted into six peaks for Ti-C 2p$_{3/2}$, Ti^{3+}/Ti^{2+} 2p$_{3/2}$, Ti-O 2p$_{3/2}$, Ti-C 2p$_{1/2}$, Ti^{3+}/Ti^{2+} 2p$_{1/2}$, and Ti-O 2p$_{1/2}$, respectively.[25, 26] Compared with $Ti_3C_2T_x$-CTAB, the proportion of Ti-O in $Ti_3C_2T_x$-CTAB-Br$_2$ was slightly increased, which was because that the end groups were oxidized by bromine to form TiO$_2$.[25] Also, except for the slightly reduced Ti-C bond, the other peaks were basically unchanged in the high-resolution C 1s XPS spectra, suggesting its high stability in bromine solution (Fig. S20b). By the way, we compared the electrochemical activity of $Ti_3C_2T_x$-CTAB and $Ti_3C_2T_x$-CTAB-Br$_2$ modified glassy carbon (denoted as TiCGC and TiCBGC, respectively), aiming to exclude the effects of the generated TiO$_2$. As shown in Fig. S20c, there was no obvious difference in CV curves of TiCGC and TiCBGC, indicating that the electrochemical activity was not affected by the slight oxidation.

Table S6 Diffusion coefficient (D_0) of Br$_2$ on PGC, TiGC and TiCGC.

Materials	PGC	TiGC	TiCGC
D_0/ cm s^{-1} × 10^{-8} (Br$_2$)	1.74	4.74	8.66

The values of D_0 are calculated from the following equation:[18]

$$I_c = 2.69 \times 10^5 A n^{\frac{3}{2}} C_0 D_0^{\frac{1}{2}} v^{\frac{1}{2}}$$

I_c: The cathodic peak current

A: The electrode surface

n: Electron transfer number

C_0: Reactant concentration

D_0: Diffusion coefficient

v: Scan rate
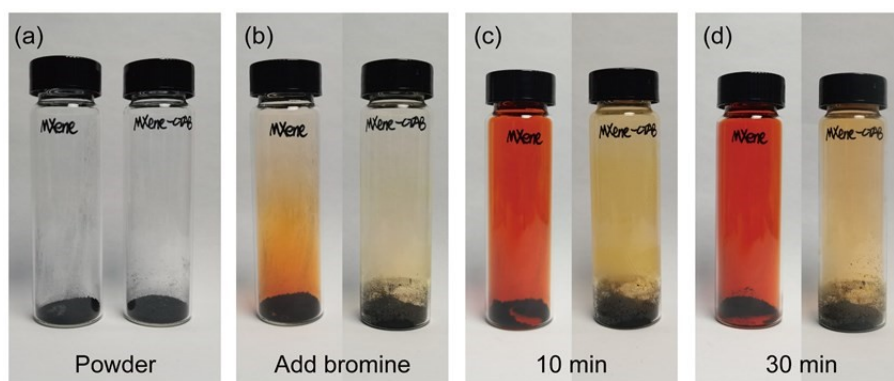
Left: Ti₃C₂Tₓ MXene Right: Ti₃C₂Tₓ-CTAB

Fig. S21 Photographs of bromine-containing Ti$_3$C$_2$T$_x$ (left) and Ti$_3$C$_2$T$_x$-CTAB (right) powder after heating at 50°C for different time.

As shown in Fig. S21a–b, when bromine was added to Ti$_3$C$_2$T$_x$ MXene powder, obvious bromine vapor was generated instantly. After being heated at 50°C, more bromine vapor was produced, indicating that the adsorption effect of Ti$_3$C$_2$T$_x$ was not stable enough (Fig. S21c–d). As for Ti$_3$C$_2$T$_x$-CTAB with the same weight, much less bromine vapor was observed at 50°C, proving that the complexation effect of CTAB was more robust (Fig. S21).

1
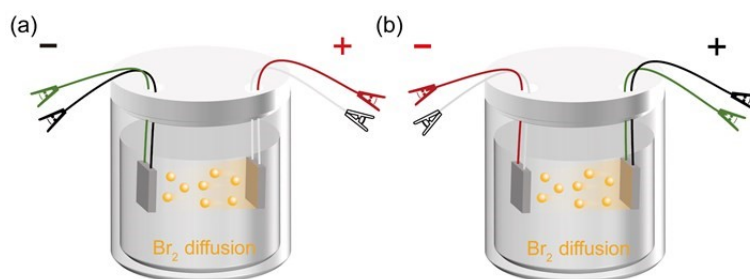
Fig. S22 Schematic diagram of the visualization experiment device in (a) Fig. S23 and (b) Fig. S24.

The colors of connecting wires in the two visualization experiment devices were not the same, however, which had no impact on the experiment results (Fig. S23-24).

5
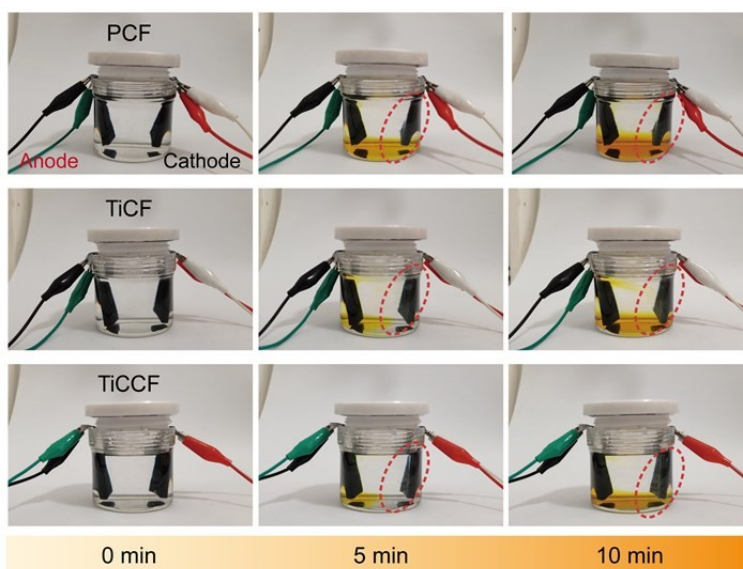
Fig. S23 Photos of the color change during charging in 2 M ZnBr$_2$ + 3 M KCl.

7
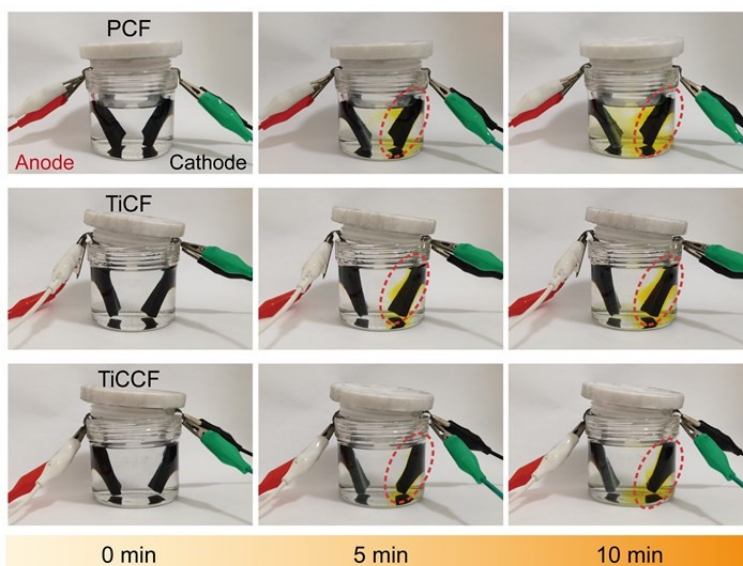
Fig. S24 Photos of the color change during charging in 2 M ZnBr$_2$ + 3 M KCl + 0.4 M MEPBr.

As shown in Fig. S23 and S24, the electrolyte at the negative side gradually turned yellow with the charge time increasing, which was due to the diffusion of bromine from the cathode surface. When using a TiCCF cathode, the color variation in the bulk electrolyte was always the slightest no matter with or without BCAs, confirming its excellent capacity to entrap and retain bromine species into the electrode.

1
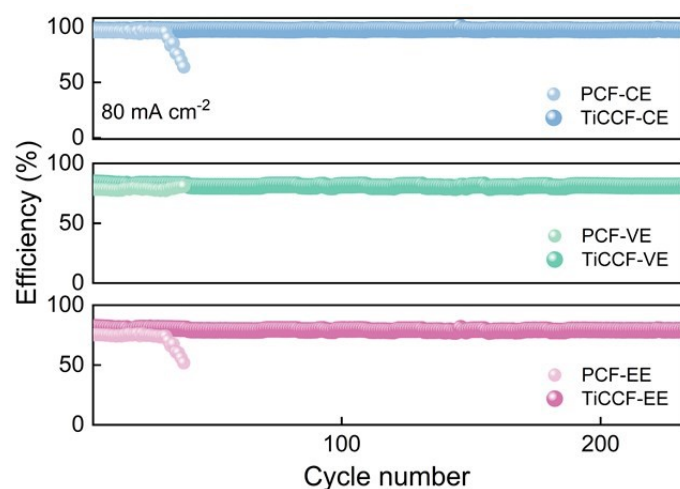
Fig. S25 Cycling performance of the ZBFBs using PCF and TiCCF cathodes (electrolytes contained no BCAs) at 80 mA cm^{-2}.

As shown in Fig. S25, at 80 mA cm^{-2}, the BCA-free ZBFB based on PCF cathode delivered a low CE of 94.18% and degraded fast due to the poor bromine entrapping/retention capacity. In contrast, the BCA-free ZBFB with TiCCF cathode could run stably for 233 cycles (232h), exhibiting higher efficiencies and reliability.

7
8
9
10
11
12
13
14
15
16
17
18
19
20
21
22
23
24
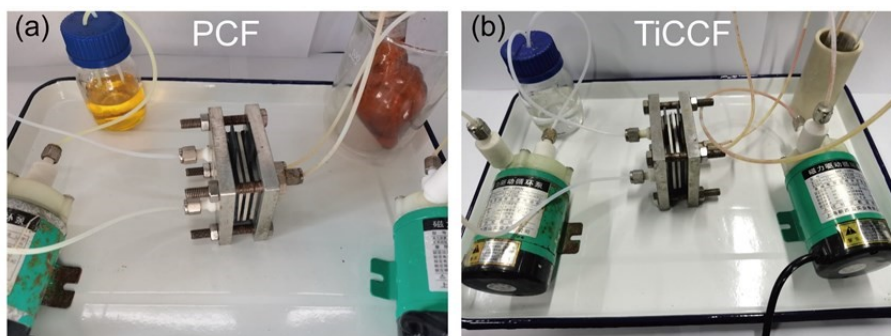
Fig. S26 The electrolyte diffusion phenomenon of the BCA-free ZBFBs using (a) PCF and (b) TiCCF as cathodes at 80 mA cm^{-2}.

Due to the poor bromine entrapping/retention capacity of PCF, the positive electrolyte diffused through the membrane to the negative side, making the negative electrolyte obviously yellow (Fig. S26a). However, in the BCA-free ZBFB assembled with TiCCF cathode, the positive electrolyte would not diffuse to the negative side during 233 cycles because bromine species could be captured into TiCCF cathode (Fig. S26b).
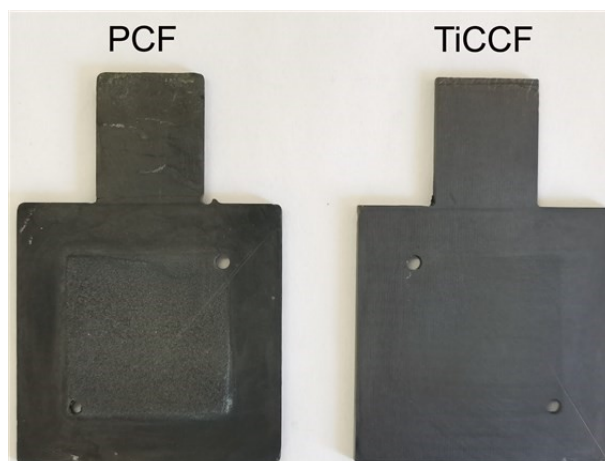
Fig. S27 Comparison of corrosion of graphite plates at the positive side of (a) PCF and (b) TiCCF electrodes after cycling at 80 mA cm⁻² when without MEPBr.

From Fig. S26a and 27, the negative electrolyte turned yellow because PCF could not entrap bromine, causing the positive current collector was seriously corroded by bromine. As expected, no bromine corrosion was observed from the positive current collector in the BCA-free ZBFB assembled with TiCCF cathode (Fig. S27).
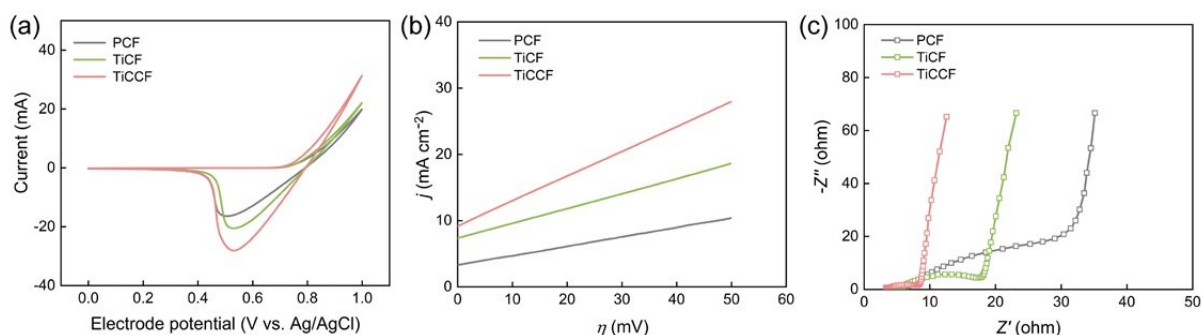
Fig. S28 Electrochemical performance of PCF, TiCF and TiCCF in 2 M ZnBr$_2$ + 3 M KCl (without BCAs). (a) CV curves at the scan rate of 10 mV s^{-1}. (b) LSV curves at the scan rate of 1 mV s^{-1}. (c) Nyquist plots.

The electrocatalytic properties of PCF, TiCF and TiCCF were also evaluated by CV, LSV and EIS in the electrolyte containing 2 M ZnBr$_2$ and 3 M KCl (without BCAs). The higher cathodic peak current (I_c) of TiCF than that of PCF suggested the high catalytic activity of Ti$_3$C$_2$T$_x$ MXene carriers on Br$_2$/Br$^-$ reactions (Fig. S28a). TiCCF exhibited the best electrochemical activity despite the solid CTA$^+$-Br$_n^-$ complexes were formed. Moreover, the slopes of the LSV curves followed the order of TiCCF>TiCF >PCF, also indicating the fastest reaction kinetics of Br$_2$/Br$^-$ couple on TiCCF (Fig. S28b). The resultant kinetic parameters were also the highest, quantifying the significant improvement in reaction kinetics (Table S7). As a result, the reaction kinetics of the Br$_2$/Br$^-$ redox couple could not be affected by solid complexation but enhanced based on the high electrochemical activity of Ti$_3$C$_2$T$_x$ MXene carriers. The smallest semicircle radius of TiCCF in the Nyquist plots also indicated the lowest charge transfer resistance and the fastest reaction kinetics of Br$_2$/Br$^-$ couple on TiCCF, supporting CV and LSV results (Fig. S28c).

Table S7 Values of R_p, i_0 and k_0 in the electrolyte without MEPBr.

Materials	R_p/ Ω cm^2	i_0/ A cm^{-2} $\times$ 10^{-3}	k_0/ cm s^{-1} $\times$ 10^{-6}
PCF	7.05	1.82	2.36
TiCF	4.45	2.88	3.74
TiCCF	2.68	4.80	6.22

The calculation methods of R_p, i_0 and k_0 were the same as in Table S5.
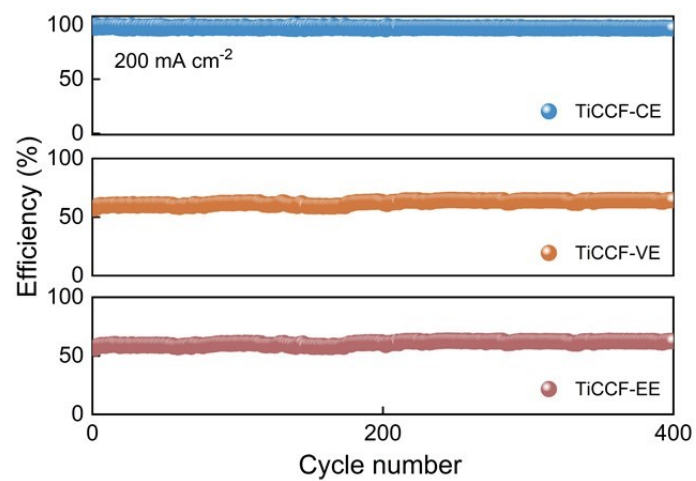
Fig. S29 Cycling performance of the BCA-free ZBFB using TiCCF cathode at 200 mA cm^{-2}.
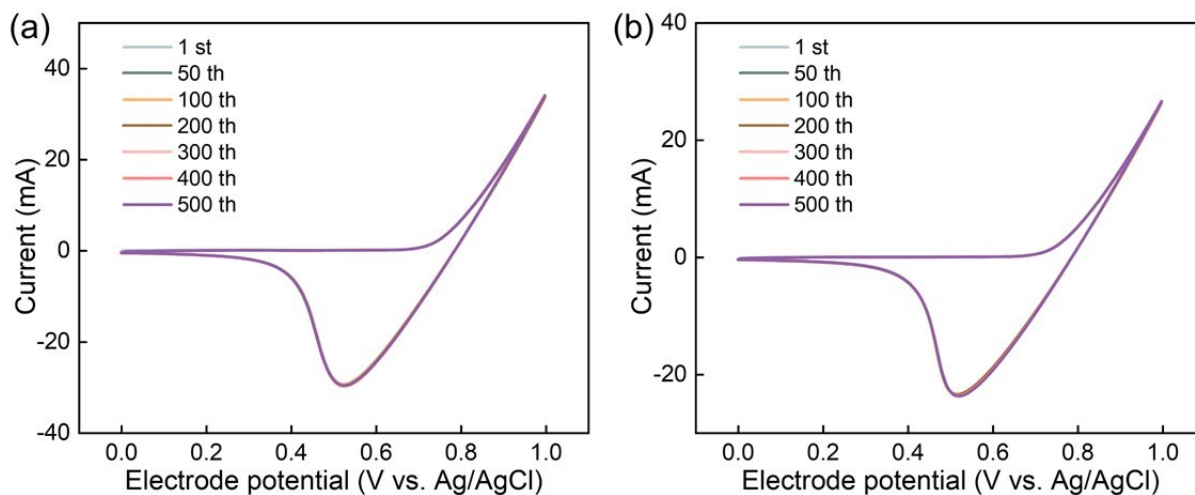
Fig. S30 CV stability test of TiCCF at the scan rate of 50 mV s⁻¹ in the electrolyte of (a) 2 M ZnBr₂ + 3 M KCl and (b) 2 M ZnBr₂ + 3 M KCl+ 0.4 M MEPBr (vs. Ag/AgCl).

The electrochemical stability of TiCCF in the electrolyte with and without BCAs (MEPBr) was measured as well. As shown in Fig. S30, the steady activity for 500 cycles demonstrated the high electrochemical stability of TiCCF in Br-FBs no matter with or without BCAs, ensuring its availability in practical applications. Notably, the I_c was significantly improved with the removal of BCAs, further proving that the addition of BCAs was unfavorable to the Br_2/Br^- redox reaction kinetics.
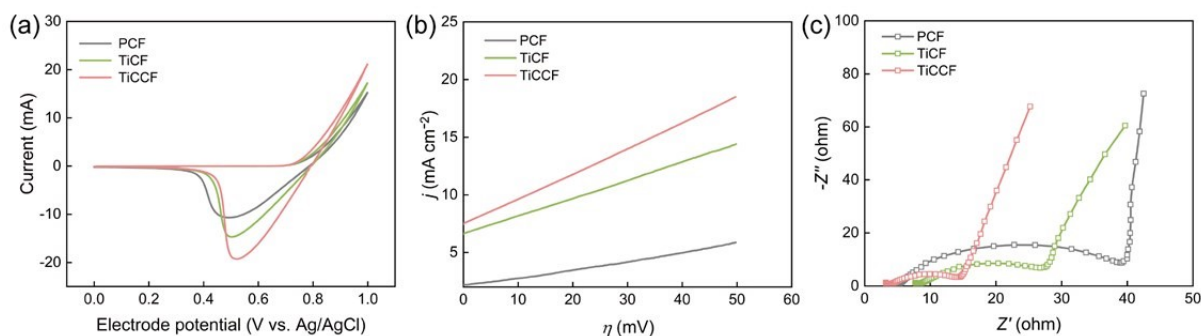
1

2 **Fig. S31 Electrochemical performance of PCF, TiCF and TiCCF in 2 M ZnBr$_2$ + 3 M KCl + 0.4 M MEPBr (with**

3 **BCAs). (a) CV curves at the scan rate of 10 mV s^{-1}. (b) LSV curves at the scan rate of 1 mV s^{-1}. (c) Nyquist**

4 **plots.**

5 The electrocatalytic performance of PCF, TiCF and TiCCF were also evaluated by CV, LSV and EIS in the

6 electrolyte containing MEPBr. As expected, TiCCF still exhibited the best electrochemical activity, the lowest

7 charge transfer resistance and the fastest reaction kinetics of the Br$_2$/Br$^-$ redox couple, contributing to the

8 lowest battery polarization (Fig. S31 and Table S8).

9

10 **Table S8 Values of R_p, i_0 and k_0 in the electrolyte containing MEPBr.**

Materials	R_p/ Ω cm^2	i_0/ A cm^{-2} $\times$ 10^{-4}	k_0/ cm s^{-1} $\times$ 10^{-6}
PCF	13.53	9.49	1.23
TiCF	6.42	20.00	2.59
TiCCF	4.54	28.30	3.67

11 The calculation methods of R_p, i_0 and k_0 were the same as in Table S5.

12 Notably, all electrodes presented worse electrochemical performance in the electrolyte with BCAs than that

13 without BCAs (Fig. S28, S30 and S31, Table S7–S8). From Fig. S28a and S31a, all electrodes in the the

14 electrolyte containing MEPBr showed much lower I_c than that without MEPBr, suggesting that the utilization

15 of BCAs reduced the catalytic activity of electrodes.[32] After removing BCAs, the reaction kinetic parameters

16 of i_0 and k_0 increased while the resistance decreased significantly (Table S7–S8).

17

18

19

20

21

22

23

24

25

1
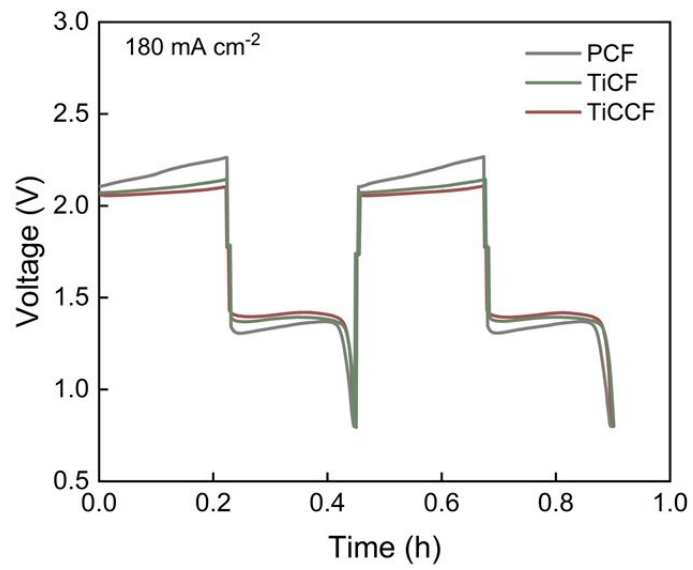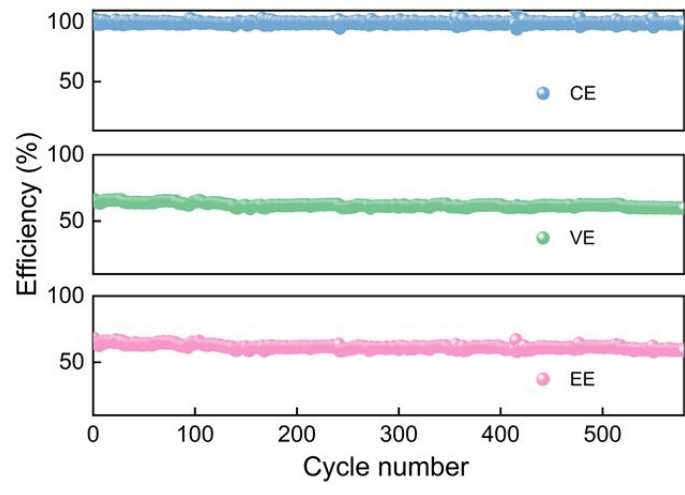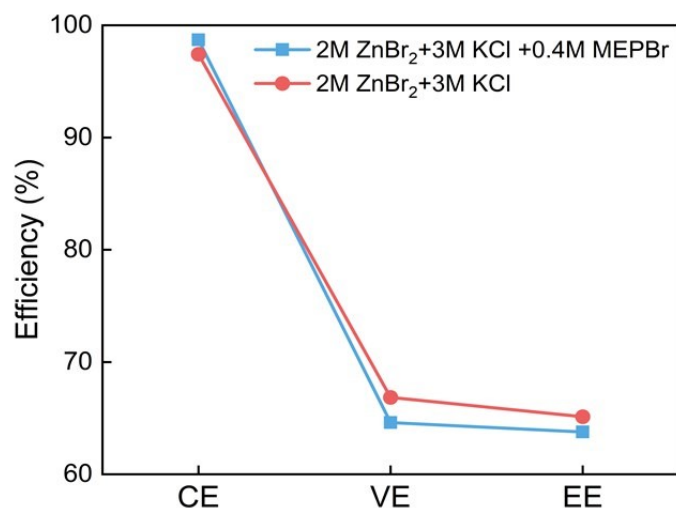
2 **Fig. S32 Charge-discharge curves of the ZBFBs using PCF, TiCF and TiCCF cathodes at 180 mA cm⁻².**

3

4

5

6

7

8

9

10

11

12

13

14

15

16

17

18

19

Fig. S33 Cycling performance of the ZBFB using TiCCF cathode at 180 mA cm^{-2}.

Fig. S34 The performance of ZBFBs assembled with TiCCF in the electrolyte with and without BCAs at 180 mA cm⁻².

As discussed above, BCAs lowered the electrolyte conductivity and exerted adverse effects on electrochemical performance.[22] As a result, the ZBFB showed an increase of 2.24% in VE and an increase of 1.36% in EE with the removal of BCAs (Fig. S34). However, the CE was decreased, which was due to less complexation of bromine when without BCAs.

1
2
3
4
5
6
7
8
9
10
11
12
13
14
15
16
17
18
19
20
21
22
23
24
25
26
27
28
29

References

1. W. Lu, P. Xu, S. Shao, T. Li, H. Zhang and X. Li, *Adv. Funct. Mater.*, 2021, **31**, 2102913.
2. G. Kresse and J. Furthmüller, *Phys. Rev. B*, 1996, **54**, 11169-11186.
3. P. E. Blöchl, *Phys. Rev. B*, 1994, **50**, 17953-17979.
4. J. P. Perdew, K. Burke and M. Ernzerhof, *Phys. Rev. Lett.*, 1996, **77**, 3865-3868.
5. J. P. Perdew, M. Ernzerhof and K. Burke, *J. Chem. Phys.*, 1996, **105**, 9982-9985.
6. S. Grimme, *Wires Comput Mol Sci*, 2011, **1**, 211-228.
7. S. Grimme, *J. Comput. Chem.*, 2004, **25**, 1463-1473.
8. E. R. Johnson and A. D. Becke, *J. Chem. Phys.*, 2006, **124**, 174104.
9. Y. An, Y. Tian, H. Shen, Q. Man, S. Xiong and J. Feng, *Energy Environ. Sci.*, 2023, **16**, 4191-4250.
10. W. I. Jang, J. W. Lee, Y. M. Baek and O. O. Park, *Macromol. Res.*, 2016, **24**, 276-281.
11. S. Suresh, M. Ulaganathan and R. Pitchai, *J. Power Sources*, 2019, **438**, 226998.
12. S. Suresh, M. Ulaganathan, R. Aswathy and P. Ragupathy, *ChemElectroChem*, 2018, **5**, 3411-3418.
13. K. Mariyappan, P. Ragupathy and M. Ulaganathan, *J. Electrochem. Soc.*, 2021, **168**, 090566.
14. R. P. Naresh, K. Mariyappan, K. S. Archana, S. Suresh, D. Ditty, M. Ulaganathan and P. Ragupathy, *ChemElectroChem*, 2019, **6**, 5688-5697.
15. K. Mariyappan, R. Velmurugan, B. Subramanian, P. Ragupathy and M. Ulaganathan, *J. Power Sources*, 2021, **482**, 228912.
16. K. Mariyappan, T. Mahalakshmi, T. S. Roshni, P. Ragupathy and M. Ulaganathan, *Adv. Mater. Interfaces*, 2023, **10**, 2202007.
17. C. Wang, X. Li, X. Xi, W. Zhou, Q. Lai and H. Zhang, *Nano Energy*, 2016, **21**, 217-227.
18. C. Wang, Q. Lai, P. Xu, D. Zheng, X. Li and H. Zhang, *Adv. Mater.*, 2017, **29**, 1605815.
19. H. Jung, J. Lee, J. Park, K. Shin, H. T. Kim and E. Cho, *Small*, 2023, **19**, 2208280.
20. H. X. Xiang, A. D. Tan, J. H. Piao, Z. Y. Fu and Z. X. Liang, *Small*, 2019, **15**, 1901848.
21. R. Wang, *J. Energy Storage*, 2023, **74**, 109487.
22. L. Tang, C. Liao, T. Li, C. Yuan, G. Li, W. Lu and X. Li, *Adv. Energy Mater.*, 2024, **14**, 2303282.
23. L. Tang, T. Li, W. Lu and X. Li, *Sci. Bull.*, 2022, **67**, 1362-1371.
24. J. Luo, C. Wang, H. Wang, X. Hu, E. Matios, X. Lu, W. Zhang, X. Tao and W. Li, *Adv. Funct. Mater.*, 2019, **29**, 1805946.
25. M. Peng, L. Wang, L. Li, X. Tang, B. Huang, T. Hu, K. Yuan and Y. Chen, *Adv. Funct. Mater.*, 2022, **32**, 2109524.
26. X. Chen, Y. Zhu, M. Zhang, J. Sui, W. Peng, Y. Li, G. Zhang, F. Zhang and X. Fan, *ACS Nano*, 2019, **13**, 9449-9456.
27. Z. Li, X. Wang, W. Zhang and S. Yang, *Chem. Eng. J.*, 2020, **398**, 125679.
28. L. Gao, Z. Li, Y. Zou, S. Yin, P. Peng, Y. Shao and X. Liang, *iScience*, 2020, **23**, 101348.
29. P. Xu, T. Li, Q. Zheng, H. Zhang, Y. Yin and X. Li, *J. Energy Chem.*, 2022, **65**, 89-93.
30. X. Li, N. Li, Z. Huang, Z. Chen, Y. Zhao, G. Liang, Q. Yang, M. Li, Q. Huang, B. Dong, J. Fan and C. Zhi, *ACS Nano*, 2021, **15**, 1718-1726.
31. X. Tang, D. Zhou, P. Li, X. Guo, C. Wang, F. Kang, B. Li and G. Wang, *ACS Central Science*, 2019, **5**, 365-373.
32. J. H. Yang, H. S. Yang, H. W. Ra, J. Shim and J.-D. Jeon, *J. Power Sources*, 2015, **275**, 294-297.